The influence of stereochemically active lone-pair electrons on crystal symmetry and twist angles in lead apatite-2H type structures

Baikie, Tom; Schreyer, Martin; Wei, Fengxia; Herrin, Jason Scott; Ferraris, Cristiano; Brink, Frank; Topolska, Justyna; Piltz, R. O.; Price, Jason; White, Timothy John

2014

Baikie, T., Schreyer, M., Wei, F., Herrin, J. S., Ferraris, C., Brink, F., et al. (2014). The influence of stereochemically active lone-pair electrons on crystal symmetry and twist angles in lead apatite-2H type structures. Mineralogical Magazine, 78(2), 325-345.

https://hdl.handle.net/10356/82237

https://doi.org/10.1180/minmag.2014.078.2.07

The Influence of Stereochemically Active Lone Pair Electrons on Crystal Symmetry and Twist Angles in Lead Apatite-2*H* Type Structures

Tom Baikie,[1] Martin Schreyer,[2] Fengxia Wei,[3] Jason S. Herrin,[3,4] Cristiano Ferraris,[5] Frank Brink,[6] Justyna Topolska,[7] Ross Piltz,[8] Jason Price[9] and T. J. White[3]

1 Energy Research Institute @ NTU (ERI@N), Research Technoplaza, Nanyang Technological University, Nanyang Drive, 637553, Singapore.

2 Institute of Chemical & Engineering Sciences, 1 Pesek Road, Jurong Island, Singapore.

3 School of Materials Science and Engineering, Nanyang Technological University, Nanyang Avenue, 639798, Singapore.

4 Earth Observatory of Singapore, Nanyang Technological University, Nanyang Avenue, 639798, Singapore

5 Laboratoire de Minéralogie et Cosmochimie du Muséum National d'Histoire Naturelle, UMR CNRS 7202, CP52, 61 Rue Buffon, 75005 Paris, France.

6 Centre for Advanced Microscopy, Australian National University, Canberra, ACT 2601, Australia

7 Department of Mineralogy, Petrography and Geochemistry, AGH-University of Science and Technology, Al. Mickiewicza 30, 30-059, Cracow, Poland

8 Bragg Institute, Australian Science and Technology Organisation, Lucas Heights, NSW 2234, Australia

9 Australian Synchrotron Company Ltd, 800 Blackburn Rd, Clayton, VIC 3168, Australia

Corresponding author: tbaikie@ntu.edu.sg

Abstract

Lead-containing (Pb-*B*-*X*)-2*H* apatites encompass a number of $[A^F]_4[A^T]_6[(BO_4)_6]X_2$ compounds used for waste stabilisation, environmental catalysis and ion conduction, but the influence of the stereochemically active lone pair electrons of Pb^{2+} on crystal chemistry and functionality is poorly understood. This article presents a compilation of existing structural data for lead apatites that demonstrate paired electrons of Pb^{2+} at both the A^F and A^T results in substantial adjustments of the Pb^FO_6 metaprism twist angle, φ. In this article, new structure refinements are presented for several natural varieties as a function of temperature by single crystal X-ray diffraction of vanadinite-2*H* (ideally $Pb_{10}(VO_4)_6Cl_2$), pyromorphite-2*H* ($Pb_{10}(PO_4)_6Cl_2$), mimetite-2*H*/*M* ($Pb_{10}(As^{5+}O_4)_6Cl_2$), and finnemanite-2*H* ($Pb_{10}(As^{3+}O_3)_6Cl_2$). A supercell for mimetite is confirmed using synchrotron single-crystal X-ray diffraction. It is suggested the superstructure is necessary to accommodate displacement of the stereochemically active $6s^2$ lone pair electrons on the Pb^{2+} that occupy a volume similar to an O^{2-} anion. We propose that depending on the temperature, and concentration of minor substitutional ions, the mimetite superstructure is a structural adaptation common to all Pb-containing apatites, and by extension apatite electrolytes, where oxide ion interstitials are found at similar positions to the lone pair electrons. It is also shown that plumbous apatite framework flex substantially through adjustments of the Pb^FO_6 metaprism twist-angles (φ) as the temperature changes. Finally, crystal chemical [100] zoning observed at submicron scales will likely impact on the treatment of diffraction data and may account for certain inconsistencies in reported structures.

1. Introduction

Apatites are a widely studied family of compounds whose general formula conforms to $A^F{}_4A^T{}_6(BO_4)_6X_2$ (A = large cations; B = metals or metalloids; X = anion). Apatites adopt a zeolitic-type topology where a flexible $A^F{}_4(BO_4)_6$ framework (F) creates one-dimensional tunnels (T), compliant with the filling characteristic of the $A^T{}_6X_2$ component. The tunnel diameter adjusts in accordance with the size (of A^T and X) and stoichiometry (of X) of its contents by counter-rotation of the opposing triangular faces of the A^FO_6 metaprism through the projected angle φ (Figure 1); the extent of metaprism twisting varies inversely with tunnel-cross section. For $P6_3/m$ structures, the twist angle varies approximately from $5^o \leq \varphi \leq 25^o$ and for apatites containing the same A^F/A^T-components, but different B and X constituents, there is a linear relationship between φ and the average crystal radii (White and Dong, 2003). Deviations from linearity usually reflect a departure from the reported stoichiometry or poor structure refinement (Lim *et al.*, 2011). As φ is established through the positions of two anions (O(1) and O(2)) that form part of the semi-rigid framework tetrahedron whose location is determined through bonding to the A^T tunnel cation, this single parameter proves exquisitely responsive to crystallochemical variations. The incorporation of divalent lead in apatites is important for environmental (White and Toor, 1996) and catalytic (Eon *et al.*, 2006) applications, but many questions remain concerning the partitioning of the Pb^{2+} over the A^F and A^T cation acceptor sites, the presence of chemical domains and zoning (Dong and White, 2004a; Dong and White, 2004b) and the role of lone pair electrons (Fleet *et al.*, 2010). In addition, all reported apatite polysomes such as ganomalite ($(Ca,Mn)_6Pb_9(Si_2O_7)_3(SiO_4)_3$ (Carlson *et al.*, 1997)), its synthetic Pb-Ge analogue ($Pb_{15}(Ge_2O_7)_3(GeO_4)_3$ (Kay *et al.*, 1975)), and nasonite ($Ca_8Pb_{12}(Si_2O_7)_6Cl_4$

(Giuseppetti *et al.*, 1971)) contain an abundance of Pb^{2+}, which suggests that the stereochemically active lone pair electrons directly influence their stability and formation (Baikie *et al.*, 2010). Depending on the polarisability of the anion coordinating to Pb^{2+}, the $6s^2$ lone-pair electrons can be stereochemically active, moderately active or inactive. This general crystal chemical behaviour has recently been reviewed for a number of oxides and chalcogenides containing bismuth, thallium, lead and tin (Walsh *et al.*, 2011). Generally, there is a preferable stereochemical inactive behaviour of lone pairs on Tl^{+} and Pb^{2+} in sulphides and sulphosalts, and the stereochemical activity is much more pronounced and more frequent in Tl^{+} and Pb^{2+} oxysalts. Andersson and Åstrom (1972), investigated the lone pair effect in some oxides and oxide-fluorides of Sb^{3+}, Bi^{3+} and Pb^{2+} and concluded that when the electron lone pairs were active, their effective volume approximated that of an O^{2-} anion. These findings were also confirmed by Moore & Shen (1984) in a subsequent study of some Pb^{2+} oxysalts. This is in contrast to semiconducting materials such as PbS (Noda *et al.*, 1987; Walsh and Watson, 2005) and $(CH_3NH_3)PbI_3$ (Baikie *et al.*, 2013) where the lone pair electrons are stereochemically inactive, or only moderately active, and the Pb^{2+} adopts a more regular coordination sphere.

In the apatite family, it is generally accepted that the lone pair electrons of Pb^{2+} are stereochemically active but to date few studies have addressed their influence on the structure and symmetry. This work uses metaprism twist angle (φ) systematics of plumbous mineral apatites to probe the crystallochemical impact of stereochemically active lone pairs on structural adaptation, by collating and comparing published data and new structure determinations. As expected, large differences in φ have been observed between Pb-apatites that contain (a) Pb in both the A^F and A^T sites, (b) Pb solely located on the A^T sites and (c) Pb-containing 'lacunar'

apatites with the *X* sites vacant and channel collapse is prevented by the Pb^{2+} $6s^2$ lone pair electrons. These differences are discussed by considering the discrete role lone pair electrons play at each acceptor site and their influence on metaprism distortion. In this way, the contrasting behaviours in φ for Pb-bearing and Pb-free apatites can be attributed to alternating orientations of the Pb^{2+} lone pair electrons at A^F positions. For mimetite, it is found that alternative positioning of the lone pair electrons gives rise to a supercell with a doubled hexagonal *a* axis compared to the conventional hexagonal $P6_3/m$ 2*H*-polytype. Previous work has suggested that the polymorph formed is dependent on temperature, with the transition temperature controlled by minor substitutional ion concentration (Keppler, 1968; Keppler, 1969). In this study, the mimetite polymorph was determined using laboratory-based and synchrotron single-crystal X-ray diffraction, and found to be comparable to the mimetite polymorph recently described by Yang *et al*. (2013). Using the revised structure for mimetite, we have revisited a series of powder synchrotron X-ray diffraction data from a synthetic mimetite-pyromorphite solid-solution and found the superstructure for mimetite persists to up to $x = 0.5$ in the $Pb_{10}(As_{1-x}P_xO_4)_6Cl_2$ series (at ambient temperature). Furthermore, natural minerals invariably contain minor elements, which for vanadinite and mimetite, result in chemical zoning at micron scales. The impact of this microstructure during structure determination and significance for apatite functionality are also considered.

2. Experimental

2.1 Mineral Samples

The minerals were drawn from the South Australian Museum and included pyromorphite ($Pb_{10}(PO_4)_6Cl_2$, G16290, Broken Hill, Yancowinna county, New South Wales, Australia), vanadinite ($Pb_{10}(VO_4)_6Cl_2$, G24999, Mibladen Mine, Upper Moulouya lead district, Midelt, Khénifra Province, Meknès-Tafilalet Region, Morocco), mimetite ($Pb_{10}(AsO_4)_6Cl_2$, G21172, Tsumeb Mine, Otjikoto Region, Namibia) and finnemanite ($Pb_{10}(AsO_3)_6Cl_2$, NRM 25397, Längban mine, Värmland, Sweden). The mineral compositions are idealised, but as discussed later; do not deviate significantly from these formulae.

2.2 Synthetic Samples

The synthesis of the $Pb_{10}(P_{1-x}As_xO_4)_6Cl_2$ (x = 0-1) solid-solution was achieved using the methodology described in Flis *et al*. (2010). Single phase samples were prepared by drop-wise mixing of aqueous solutions of $Pb(NO_3)_2$, KCl and/or K_2HPO_4 and/or $Na_2HAsO_4{\cdot}7H_2O$ in molar proportions based on the stoichiometry of the target material. Suspensions of the precipitates were stirred using a mechanical stirrer for 5h and allowed to settle. Following 2 weeks of reaction the precipitates were separated from the solutions by decanting. The products were washed with distilled water and acetone, and dried at 383K for 12 hours.

2.3 Single Crystal X-ray Diffraction (*Bruker Smart Apex II)*

Data were collected at room temperature and 100 K with a Bruker Smart Apex II three-circle diffractometer using graphite monochromated Mo-*Kα* radiation (λ = 0.71073 Å). The Saint module, deployed within Apex II was used for reflection integration, and performing Lorentz

polarisation and multi-scan absorption corrections. Structure determinations were performed with Jana 2006 (Petriček *et al.*, 2006) utilising the Superflip (Palatinus and Chapuis, 2007) structure solution algorithm. Three-dimensional difference Fourier maps were generated with VESTA (Momma and Izumi, 2008).

2.4 Synchrotron Single Crystal X-ray Diffraction (MX1 beamline)

Single crystal diffraction measurements were carried out on a crystal of mimetite (crystal dimensions (10 μm × 10 μm × 2 μm) at the MX1 beamline of the Australian Synchrotron operated at a wavelength of 0.71073 Å. Scans in φ were recorded with an angular step of 2º, and integration time of 1s per step. Diffraction patterns were accumulated with an ADSC Quantum 210r detector positioned 72.070 mm from the crystal. The reduction of the single crystal data was carried out using the XDS package (Kabsch, 2010) and refined with Jana 2006 (Petriček *et al.*, 2006).

2.5 Powder Synchrotron X-ray Diffraction

Powders were mechanically ground in an agate pestle and mortar then passed through a 20μm sieve. Charges of approximately 2.5mg were loaded and sealed in 2mm diameter Kapton tubes, then mounted on bases provided by the 11-BM beamline at the Advanced Photon Source. The diffraction patterns were collected at ambient temperature using monochromatic synchrotron radiation of wavelength 0.4015 Å. Raw data from each of the 12 detectors were calibrated, merged and reduced using in-house routines (Lee *et al.*, 2008). Experimental fitting of the X-ray

data was carried out from 2-40° 2θ using *TOPAS V4.1* (Bruker, 2008). The background was fitted using 10 terms of a Chebyshev polynomial, with a pseudo-Voigt peak shape corrected for asymmetry.

2.6 Analytical Scanning Electron Microscopy

An Hitachi 4300 SE/N field emission scanning electron microscope (FESEM) fitted with an Oxford Inca X-ray analysis system and a light element SiLi detector was used to determine the chemical composition of the pyromorphite, vanadinite, mimetite and finnemanite. The energy dispersive X-ray spectra (EDX) data were collected at 15kV with a probe current of 0.6nA and a minimum of 10 points across a large crystal embedded in an epoxy resin disk polished to a mirror finish using 0.5μm diamond paste. The constituent elements were calibrated against the following standards; CeP_5O_{14} (P), NaCl (Cl), GaAs (As), V metal (V), $PbCrO_4$ (Pb). Initial oxygen analyses were calculated by stoichiometry based on the known valence state of the cations, then recalculated to correct for chlorine.

2.7 Electron Probe Microanalysis (EPMA)

Quantitative WDS analyses were performed using a JXA-8530F Field Emission Electron Probe X-ray Microanalyser (FE-EPMA). Point analyses were acquired using a 10 μm diameter defocussed beam at a probe current of 20 nA and an accelerating voltage of 6 kV. Results were quantified using external calibration standards and a ZAF matrix correction procedure (Philibert & Tixier, 1968, Philibert, 1963, Reed, 1965). Error on repeat analysis of standards was <2% of

measured values. The following X-ray lines were monitored with the appropriate spectrometer crystals, as indicated, for fixed peak counting times: O K_α (LDE-1, 30s), F K_α (LDE-1, 150s), Cl K_α (PET-J, 60s), As L_α (TAP-H, 20s), Pb M_α (PET-H, 20s), P K_α (PET-H, 150s), Ca K_α (PET-H, 100s), Si K_α (PET-H, 100s). Background measurements were performed on either side of each peak position for combined background counting times equalling the corresponding peak counting times. The following external calibration standards were used: crococite (Pb, O), fluorite (F), tugtupite (Cl, Si), skutterrudite (As), apatite (Ca, P). Peak and background regions were found to be interference-free, with the exception of Cl *K*α. The possibility of Pb *M*-line interferences on Cl *K*α was evaluated using a crococite mineral standard, and found to be <1% of Cl measurements at the Pb and Cl content of mimetite samples analysed.

A second set of quantitative analyses was also performed to evaluate the abundance of trace elements. In this instance, an accelerating voltage of 25kV and a beam current of 40 nA was used with a defocussed 10 µm diameter beam rastered over a 50 µm × 50 µm area to minimise beam damage. A ZAF matrix correction procedure was used to quantify these results wherein the major element composition (Pb, As, O, Cl) were fixed at stoichiometric values. The collection conditions were: F K_α (LDE-1, 300s), V K_α (LIF, 300s), Na K_α (TAP-H, 30s), Mg K_α (TAP-H, 150s), Si K_α (PET-H, 100s), Ti K_α (PET-H, 100s), Sb L_α (PET-H, 100s), S K_α (PET-H, 100s), P K_α (PET-H, 100s), Ca K_α (PET-H, 100s) and background measurements accumulated as described earlier for the major elements . The following external calibration standards were used: fluorite (F), vanadium (V), kaersutite (Na, Mg, Si, Ti), antimony telluride (Sb), galena (S), apatite (Ca, P). Peak and background regions did not interfere, because these analyses did not reveal elements not quantified previously at 6 kV/20 nA beam conditions. The detection limits

for these analyses are combined with previously determined concentration values and reported together (Table 4).

In order to evaluate the possible presence of unknown chemical components, qualitative analyses were also performed by EPMA. Ten locations were analysed on two separate specimens using Wavelength-Dispersive X-ray Spectroscopy (WDS) at an accelerating voltage of 30 kV and a beam current of 40 nA. During these analyses, available diffraction crystals (LDE, TAP, PET, and LIF) were cycled through their entire range of movement at a step interval of 50 µm and a dwell time of 100 ms at each step. These analytical procedures cover nearly the entire periodic table from C to U (Z = 6-92). Detection limits vary by element and are also unique to each analysis. Under the analytical conditions used, detection limits of 10-1000 ppm were achieved for all relevant elements.

In order to evaluate the spatial distribution of minor components, X-ray elemental maps were collected with a stationary focused beam at 15 kV and 80 nA and continuous stage motion resulting in 75 ms dwell times for each 1 µm × 1 µm pixel area. Spectrometers remained fixed at the following X-ray peak positions: Si K_α (TAP), Cl K_α (PET-J), O K_α (LDE1-H), P K_α (PET-H), Ca K_α (PET-H).

2.8 Electron Backscattered Diffraction

The mimetite crystal orientation was determined using a JEOL JSM-7600F Field Emission Scanning Electron Microscope (FESEM) equipped with an Oxford/HKL electron backscatter

diffraction (EBSD) system in the Facility for Analysis, Characterisation, Testing, and Simulation at Nanyang Technological University. Diffraction patterns were indexed to the hexagonal mimetite structure reported by Dai *et al.* (1991).

3. Results & Discussion

3.1 Single Crystal X-ray Diffraction

3.1.1 Vanadinite – $[Pb_4]^F[Pb_6]^T(VO_4)_6Cl_2$

The structure of vanadinite first reported by Trotter and Barnes (1958) was essentially confirmed by Dai and Hughes (1989), but with improvement in the Pb-O and V-O bond lengths due to enhanced data collection. The present refinements (Tables S1-4) agree with the latter but with metal-oxygen bond lengths refined to greater precision, and small differences in the V-O distances, lead to slightly more distorted tetrahedra than previously found (c.f. Dai and Hughes V-O(1),(3) = 1.70(1) Å, V-O(2) = 1.69(1) Å), although this may be an artefact of the V/P zoning (see section 3.4) or that the VO_4 tetrahedra are more readily deformed than P/AsO_4 tetrahedra. However, such questions are not readily answered. Anisotropic refinement of the ADPs in the 100 K dataset gave a non-positively defined value for the V^{5+} site, possibly arising from V/P chemical zoning seen in the compositional X-ray maps, or reflecting that vanadinite undergoes polymorphic conversion as found for mimetite and suggested for pyromorphite (see below). To determine possible locations for the Pb^{2+} $6s^2$ lone pair electrons in vanadinite the refined structural information was transferred to *ATOMS* (Dowty, 2002) and by using realistic ionic radii

(Shannon, 1976), the cavity calculation feature was used to identify void space. Figure 2a shows a representation of vanadinite with structural voids having a radius > 0.6 Å (grid spacing 0.1) drawn in yellow at positions close to the Pb^{F} and Pb^{T} sites. The former type of void resides between the VO_4 tetrahedra with fractional coordinate close to [0 ½ 0] and the latter within the channel at a position centred at [0.0288 0.8365 0.2568]. It is probably not coincidental that these two potential lone pair positions essentially correspond with interstitial superstoichiometric oxygen found in the apatite oxide ion conducting electrolytes (Béchade *et al.*, 2009; León-Reina *et al.*, 2004; Orera *et al.*, 2011; Panchmatia *et al.*, 2001). Both voids are found to have a maximum radii of approximately 0.75 Å. Although the lone-pair electrons may not be positioned exactly at the sites suggested, it is believed that the loci of the lone-pair electrons from the Pb^{2+} are directed towards these voids. The atomic positions of all voids greater than 0.74 Å are listed in Table S5.

3.1.2 Pyromorphite – $[Pb_4]^{F}[Pb_6]^{T}(PO_4)_6Cl_2$

Pyromorphite was one of the earliest apatite structure determinations (Hendricks *et al.*, 1932) that was not revisited for almost 60 years (Dai and Hughes, 1989). More recently, Mills *et al*. (2012) described the first documented case of {10-10 twinning by reflection (or by twofold rotation about [100]) of merohedry (class II) in the apatite supergroup by investigating a sample of pyromorphite. Vanadinite and pyromorphite are isomorphous with obvious differences in tetrahedral distortion arising from the *B* cations (V^{5+} = 0.36 Å; P^{5+} = 0.17 Å), in agreement with Dai & Hughes (1989) (Tables S6-9). Analytical SEM showed pyromorphite to be compositionally stoichiometric within the analytical precision of the technique (< 0.1wt%),

consistent with the small spread of P-O bond lengths and ADPs of the slightly distorted tetrahedron. This is in contrast to the irregular tetrahedral environment found for the chemically zoned vanadinite. In this study, single crystal X-ray diffraction study yielded physical ADPs at room temperature but unusually, the *R* factors and GoF were larger for the 100 K data set and the ADPs for the Pb(1), P and O(3) positions became non-positively defined. Given the crystal analyses as stoichiometric (section 3.4) this implies a temperature driven change in crystal symmetry, possibly similar to the mimetite superstructure described below. In addition, Figure S1 shows a three dimensional difference Fourier map from the X-ray diffraction data collected at 100 K. The main peaks of excess electron density surround the Pb^{F} site, suggesting the Pb^{2+} ions are displaced from the 4*f* Wyckoff position in $P6_3/m$ in the *a*-*b* plane, consistent with a lower-symmetry structure. Cavity calculations for pyromorphite at room temperature were essentially the same as for vanadinite, but the voids were slightly smaller, reflecting the difference in ionic radii between P^{5+} (0.17 Å) and V^{5+} (0.34 Å).

3.1.3 Mimetite - $[Pb_4]^{F}[Pb_6]^{T}(AsO_4)_6Cl_2$

Natural mimetite is reportedly polymorphic, and aside from the usual $P6_3/m$ symmetry at room temperature (Dai *et al.*, 1991; Sokolova *et al.*, 1982), also adopts the less well characterised 'clinomimetite' (the mineral name clinomimetite was recently abandoned in favour of mimetite-2*M* (Pasero *et al.*, 2010)) polymorph in the space group $P112_1/b$. This monoclinic polymorph is less well characterised but contains displacements of the locus of the stereochemically active Pb^{F} lone pair electrons (Dai *et al.*, 1991). The $P112_1/b$ monoclinic form is apparently rare, and was discovered by investigating 10 alternative crystals from different

localities. Only one of these crystals displayed the monoclinic structure and it was suggested that it is stabilised by minor isomorphic substitutions (e.g. Ca^{2+}, P^{5+} and O^{2-}) or non-stoichiometry. This interpretation was supported by a temperature dependent powder neutron diffraction study of a synthetic mimetite ($Pb_{10}(AsO_4)_6Cl_{1.48}O_{0.26}$) (Baikie *et al.*, 2008) that found no evidence of a phase transformation from 293-473K. However, refinement of the O(2) and O(3) across split sites was necessary to enable a satisfactory fit to the data. In addition, a more recent powder X-ray synchrotron study of synthetic $Pb_{10}(AsO_4)_6Cl_2$ found $P6_3/m$ to be an appropriate space group (Flis *et al.*, 2010), however, additional un-indexed reflections were identified in the diffraction patterns that were presumed to result from an undetected secondary phase. Furthermore, a single crystal neutron diffraction of mimetite revealed unusually large anisotropic displacements for the oxygen sites but no explanation was given (Calos and Kennard, 1990).

Initial refinements for mimetite were performed on the room temperature data set in $P6_3/m$ but it was clear that the refinement residuals were systematically higher than those found for vanadinite and pyromorphite (see Tables S10-13). In addition, the refined APDs at room temperature gave non-positively defined values for the As, O(1) and O(2) sites (see Table S11). Furthermore, the ionic radii of V^{5+} (0.36 Å) and As^{5+} (0.34 Å) are similar, so size considerations alone would suggest that mimetite shows similar phase transition behaviour to vanadinite, although this may be modified by the differences between the electronic structures of V^{5+} and As^{5+}.

Refinements were attempted in lower symmetry sub-groups of $P6_3/m$, but these offered no significant improvement to the data fitting, or the residuals. It was initially suspected that the poor fit could be due to the presence of significant quantities of impurity ions, however, analytical SEM of a large crystal found the mineral is compositionally stoichiometric within the precision of the technique (<0.1wt% (see section 3.4)); subsequent EPMA found minor substitution up to a maximum 0.19(4) wt% for Ca, 0.07(3) wt% for P. Refinements in $P6_3/m$ at room temperature could not account for electron density at distances close to existing atomic sites, with the magnitude of these Fourier peaks and poor refinement indices increasing substantially at 100K (see $P6_3/m$ refinement details at RT and 100K in Tables S11-S12).

Single-crystal X-ray diffraction data were collected from a fragment of mimetite crystal on the MX1 beamline at the Australian Synchrotron. The data were indexed in a monoclinic cell (see Table S14) with a doubled *a* and b parameters relative to the aristotypic hexagonal $P6_3/m$ apatite cell. Figure 3 shows views of reciprocal space for I_{obs} along b^* at a) $k = 0$ and b) $k = 3$. All the even numbered reflections (h 0 l) and (h 3 l) correspond to conventional apatite cell while the odd numbered reflections correspond to the supercell. This enlarged cell is in close agreement to that recently reported by Yang *et al*. (2013), however, the systematic absences for the current data collection suggested the higher symmetry space group $P2_1/a$ compared to $P2_1$ in the previous work. The inclusion of the additional symmetry elements reduces the number of atomic positions by 50% compared to the $P2_1$ model. The Superflip structure solution algorithm (Palatinus and Chapuis, 2007) identified the ten Pb^{2+} and six As^{5+} positions, with the O and Cl sites ascertained from the difference Fourier maps. The refinement proceeded smoothly to yield much more acceptable reliability indices and goodness-of-fit. The refinement details, atomic

positions, anisotropic atomic displacement parameters and selected bond lengths are listed in Tables S14-16. Note that the monoclinic cell is in its standard setting with the screw diad ∥ *b*. Hence, the space group symbol is $P12_1/a1$ and the doubled cell parameters are *a* and *c*. The high quality fit indicates a much more acceptable model for mimetite compared to that obtained in the conventional hexagonal cell. All atomic displacement parameters are positive-definite in the supercell, and no strong features of electron density were observed in the difference Fourier maps. Figure 2b & S2 show a structural representation of the mimetite supercell. The main difference between the hexagonal $P6_3/m$ and $P2_1/a$ models is the coordination of the Pb^F ions. In the hexagonal $P6_3/m$ structure, the Pb^{2+} is nine-coordinate, with six Pb-O bonds forming a distorted metaprism and three longer Pb-O bonds (≈ 2.9 Å) completing the coordination sphere. In the supercell, this Pb^F coordination is heavily distorted and for the $Pb^F(1)$ site in particular, the coordination might be better described as 8 + 1 (green polyhedra in Figure 2b). The AsO_4 tetrahedra adjacent to the $Pb^F(1)$ polyhedra contains an oxygen with a bond distance ($Pb^F(1)$-O(6d) = 3.340(6) Å) that is significantly than the other Pb-O distances (see Table S16) and comparable to the Pb(1)-As(4) distance of 3.3645(10) Å, so it is difficult to rationalise it as a significant chemical bond. Using the same method as for vanadinite, the cavities within the structure (Figure 2b) were calculated for voids of radii greater than 0.55 Å; and the fractional coordinates of all voids greater than 0.72 Å are listed in Table S17. The void circled in red in Figure 2b presumably accommodates the lone pair of Pb^{2+}, which explains the tilt of the adjacent AsO_4 tetrahedra away from the Pb coordination sphere. The location of the lone pair near the tilted tetrahedra is also inferred from the displacement Cl ion in the nearby channel. It is also clear that there are two alternative arrangements of the Cl channel ions in adjacent layers, where one shows a near-linear arrangement of Cl as found in conventional hexagonal apatites (Figures

2 & S2). Although $P2_1/a$ was selected as the most appropriate space group for the present analysis, further distortion of the structure could lead symmetry reduction to the non-isomorphic subgroups $P2_1$ or P-1.

3.1.4 Finnemanite

Finnemanite, $Pb_{10}(AsO_3)_6Cl_2$ is a partially reduced apatite with a structure closely related to mimetite $Pb_{10}(AsO_4)_6Cl_2$, but whereas the latter contains pentavalent arsenic in tetrahedral coordination, finnemanite accommodates trivalent arsenic in triangular pyramidal coordination. Simply, finnemanite is derived from mimetite by removal of an oxygen from the tetrahedron and simultaneous reduction of As^{5+} to As^{3+} (Figure 4). Finnemanite, which has few natural occurrences (Aminoff, 1923; Elliott, 1991; Grubb, 1971), was soon recognised as bearing a possible structural relationship to mimetite by Aminoff & Parsons (Aminoff and Parsons, 1927). Subsequently, the crystal structure of finnemanite was determined in the space group $P6_3$ (Gabrielson, 1955), however, a re-determination gave the symmetry as $P6_3/m$ (Effenberger and Pertlik, 1979). We have recently reported the synthesis and crystal chemistry of a synthetic samples of finnemanite (Baikie *et al.*, 2008) and although unidentified impurities in the sample hindered detailed structural characterisation, we found $P6_3/m$ to appropriately describe the Bragg reflections of the powder neutron diffraction data. However, a recent Raman spectroscopy study of a single crystal of finnemanite (Bahfenne and Frost, 2010) showed four anti-symmetric stretching vibrations, which suggests the presence of non-equivalent AsO_3 units. This evidence is consistent with finnemanite belonging to a lower symmetry system than $P6_3/m$, which only allows for one AsO_3 environment, with diffraction experiments indicating the average symmetry.

Our crystallographic study of finnemanite collected from the Längban mine, Värmland, Sweden is in general agreement with the original work carried out by Effenberger and Pertlik (1979). We found that $P6_3/m$ offered a reasonable fit to the room temperature data, but as found for mimetite, the goodness-of-fit and reliability indices increased substantially in the 100K dataset, which showed non-positive definite ADPs for all atomic positions (see Table S20). Figure 4 shows a structural representation of the room temperature refined structure of finnemanite. Finnemanite could possibly adopt a superstructure similar to that for mimetite, however, further diffraction studies will be required to confirm an alternative cell, which would probably necessitate the use of intense synchrotron radiation to reveal any supercell reflections. Figure S3 shows substantial excess electron density in the difference Fourier maps that were calculated from the refinements performed at 100K. Refinement details and selected bond lengths for the refined structure of finnemanite are listed in Tables S18-21.

3.2 Bond valence sums (BVS)

Jana 2006 found that the BVS deviate from the expected values (Table 1). Those for vanadinite are closest to the ideal values but with the V^{5+} and O(2) sites slightly overbonded. For the pyromorphite, the P, O(1) and O(3) sites are slightly underbonded with the O(2) and Cl over-bonded. In the hexagonal mimetite models, the As^{5+} in mimetite deviates most from the ideal values with the O(2) site also overbonded, while both the Pb^F and Pb^T sites are underbonded. For the finnemanite the Pb^F site is under-bonded with the As^{3+}, O(1) and Cl sites significantly overbonded. As expected, the bond valence sums for the mimetite supercell are

much more satisfactory, particularly for As^{5+}, that within experimental error does not deviate from the ideal value of +5 (see Table 2). The O(3d) site has an unusually low bond valence sum of 1.74(2) but this oxygen site also has the highest isotropic displacement, which may indicate that symmetry changes at lower temperature. Overall inspection of the refinement parameters for the enlarged cell for mimetite confirms a superior-quality refinement relative to the conventionally accepted model.

3.3 Reanalysis of the Powder Synchrotron X-ray Diffraction data for the Synthetic $Pb_{10}(P_{1-x}As_xO_4)_6Cl_2$ Solid-Solution

Recently Flis *et al*. (2010) reported a powder X-ray synchrotron diffraction study of the synthetic pyromorphite-mimetite solid solution ($Pb_{10}(P_{1-x}As_xO_4)_6Cl_2$). In this work, additional reflections were assigned to an impurity phase not detected in conventional laboratory-based powder X-ray experiments. Here, we have reanalysed these data using the revised monoclinic model for mimetite, which confirms that the additional reflections are associated with mimetite and not impurity phase(s). The refinement profile is shown in Figure 5 and the insert shows an expanded region highlighting the reflections inconsistent with the formerly accepted hexagonal $P6_3/m$ model. Comparison of the reliability indices for the monoclinic and hexagonal models reveals a superior fit with the former ($P6_3/m$: R_{exp} = 5.40, R_{wp} = 14.37 R_p = 10.67, R_{Bragg} = 4.719, *GoF* = 2.66; $P12_1/a_1$: R_{exp} = 5.40, R_{wp} = 11.57 R_p = , R_{Bragg} = 3.653 , *GoF* = 2.143. Additionally, the supercell is found to persist until approximately the $Pb_{10}(P_{0.5}As_{0.5}O_4)_6Cl_2$ member of the series (Figure 6). The (1 -1 -3) reflection is one of the most intense of the supercell reflections in Figure 6, and its intensity diminishes with increasing x until it is not detected for $x \geq 0.5$. The

supercell reflections are of very low relative intensity and the *y* axes of the diffraction data in Figure 5 & 6 are displayed as logarithm of intensity to enhance their appearance. The diffraction data were all collected at room temperature, and although further experimental work is needed, we postulate that the supercell will be both compositionally and temperature dependent, and it may persist beyond $x = 0.5$ if the temperature is reduced below ambient. This suggestion is supported by the changes observed in the single crystal X-ray diffraction data for the mineral pyromorphite and mimetite samples, where the 100 K data collections gave poorer fits and a corresponding increase in excess electron density in the difference Fourier maps, particularly near the Pb^{2+} sites. Plots of the lattice parameters in hexagonal symmetry were reported in Flis *et al*. (2010), which showed that the variation in the *a* lattice parameter was essentially linear but there was a slight deviation from linearity for the *c* axis for values of $x > 0.5$ in the $Pb_{10}(As_{1-x}P_xO_4)_6Cl_2$ system. This is in good agreement with the appearance of the mimetite superstructure in the present re-analysis of the diffraction data. Following from the current analysis, it is reasonable to speculate that at room temperature the $Pb_{10}(As_{1-x}V_xO_4)_6Cl_2$ solid-solution will also show superstructure reflections for compositions with a greater concentration of As^{5+}, and further experiments are planned to verify this. Additional validation of polymorphism may come from variable temperature powder X-ray diffraction studies on the $Pb_{10}(As_{1-x}P_xO_4)_6Cl_2$ and $Pb_{10}(V_{1-x}P_xO_4)_6Cl_2$ with intense synchrotron radiation to reveal the supercell reflections.

3.4 Elemental Analysis and Chemical Zoning of Apatites

As minerals invariably contain minor substitutional ions that may induce or suppress phase transformations, quantitative microanalysis is essential. The vanadinite, pyromorphite, mimetite and finnemanite were analysed using EDX, while the mimetite was additionally verified using EPMA. Another purpose of the analysis was to show that the minerals studied were close to stoichiometric, and any phase transformations observed were inherent to the material and therefore could be expected in synthetic samples.

All the minerals studied in this work were verified as close to stoichiometric. The SEM/EDX analysis for the vanadinite, pyromorphite, mimetite and finnemanite are shown in Table 3 and for the pyromorphite and mimetite no elements were detected other than those expected. For the vanadinite, trace quantities of P were observed up to a maximum 0.1-0.4 wt % and for the finnemanite, trace amounts of Fe (0.1-0.2 wt%) and Sb (0.2-0.3 wt %) were detected. Note that these values are however close to the detection limit, and so should be treated as indicative rather than absolute. For the vanadinite, the minor P^{5+} content was found to be zoned (Figure 7 a & b).

EPMA of Mimetite

As the mimetite was confirmed to display a superstructure, this material was additionally analysed using EPMA, which has a superior lower limit of detection. In contrast to the SEM analysis, the EPMA of the mimetite revealed minor Ca^{2+} and P^{5+}, which also exhibited zonation. The origin of the chemical zonation in both vanadinite and mimetite is beyond the scope of the present article but it is a commonly observed phenomenon in minerals. For further information

on the topic of chemical zonation in minerals the reader is directed to the following excellent reviews (Holten *et al.*, 2000; Shore and Fowler, 1996).

Wavelength-dispersive electron microprobe analysis of the mimetite detected major Pb, As and Cl, together with lesser quantities of Ca and P. Full details of the major and minor elements of the elements quantified in the EPMA analysis are shown in Table 4. Nitrogen was also observed sporadically within the sample, but is unlikely to be a crystalline constituent, and rather trapped gas bubbles. X-ray elemental mapping shows concentric oscillatory chemical zoning with interfaces parallel the external faces of crystals. An inverse correlation was seen between concentrations of Ca and P. EBSD observations confirm that bands are thickened parallel to the fast-growth direction of the *c*-axis, an indication that this banding is a primary feature, likely the result of chemical or thermal changes in the environment during crystal growth. The *c*-axis of the mimetite crystal in Figure 7c & d is inclined at 40.5° (±0.5) to the plane of the sample surface.

3.5 Twist Angle Systematics

In the present structure determinations, vanadinite gave the smallest twist angle for the A^F metaprism at room temperature with φ = 17.1°, and was found to decreases to 16.0° at 100K. The magnitude of twist angle reflects the structural distortion, and for apatites with the channel site tenanted at [0 0 ¼] the maximum twist angle is 24-25° before bond valence requirements and tetrahedral tilting requires that apatites undergo a distortion to triclinic symmetry e.g. $Ca_{10}(BO_4)_6F_2$ (*B* = As and V) (Baikie *et al.*, 2007). A recent analysis of the mineral johnbaumite $Ca_{10}(AsO_4)_6(OH)_2$ (Biagioni and Pasero, 2013) showed this species adopts hexagonal symmetry.

Although OH^- and F^- are similarly sized, the slightly larger OH^- units (F = 1.33 Å, OH = 1.37 Å) are necessarily displaced along the channel from [0 0 ¼] for F to 0 0.216(3) for OH^- to satisfy the bond valance requirements, which results in a lower twist angle of 21.2°. As vanadinite has the smallest twist angle it follows that this mineral has the least distorted structure, which is consistent with the present study. As expected, the room temperature structure of mimetite data gave the largest twist angle with φ = 18.3°, which is also the largest of any Pb containing apatite where the channel ion is positioned at the origin. The $Pb_{10}(PO_4)_6O$, $Pb_{10}(PO_4)_6(OH)_2$ and $Pb_{10}(PO_4)_6F_2$ apatites all have larger φ than mimetite, but for these, bond valence requirements result in the channel ions being displaced along the tunnel to 0 0 *z* ($z \approx 0.13$ for O^{2-} and OH^- and $z = 0.25$ for F). At 100 K the twist angle for mimetite reduced slightly but remains larger than either the pyromorphite (RT φ = 17.8°; 100 K = 17.3°) or the vanadinite. The difference in response to cooling strongly indicates that the hexagonal $P6_3/m$ model for mimetite is incorrect. The smaller twist angle at lower temperatures for all the minerals is consistent with the channel contracting less than the framework.

Crystallographic data for all known Pb containing apatites obtained reliably using by single crystal X-ray diffraction, and powder X-ray and neutron diffraction and compiled in Table 5 (the cation distributions for the synthetic $Pb_{10-x}Ca_x(VO_4)_6F_2$ from Dong & White (2004a; 2004b) are shown in Table 6). Figure 1 shows a polyhedral representation of the two extremes of twist angle found in Pb containing apatites. The twist angles vary in accord with the *A* and *B* framework/tunnel radius ratios. However, when Pb^F is completely replaced by other ions, there is a dramatic reduction in the twist angle e.g. $Ca_2Na_2Pb_6(PO_4)_6$ (φ = 9.7°) and $Ca_2Li_2Pb_6(PO_4)_6$ (φ = 13.6°). A similar situation is found for hedyphane (Rouse *et al.*, 1984) and

phospohedyphane (Kampf *et al.*, 2006), where Pb^{2+} is absent at the A^F sites. Compared to apatites with the A^F site fully occupied by Pb, φ is ~8° lower. Apatites that contain less than 50% occupancy of Pb on the A^F site show a decreasing trend in twist angle as the size of the tunnel becomes larger with respect to the framework, but they are all less than those apatites with ≥50% occupancy of Pb in the A^F sites. It can be concluded that the lack of lone pairs results in smaller twist angles.

When structural representations of apatites that contain Pb or alternative ions on the A^F or A^T sites are compared, the dependence of twist angle becomes clearer. Figure 8 shows drawings of $Pb_9(PO_4)_6$, $Pb_{10}(PO_4)_6Cl_2$ and $Ca_4Pb_6(PO_4)_6Cl_2$ and $Ca_{10}(PO_4)_6Cl_2$ using absolute relative ionic radii (Shannon, 1976). For the apatites that contain Pb on the A^F site, i.e. $Pb_9(PO_4)_6$ and $Pb_{10}(PO_4)_6Cl_2$, there appears to be a small displacement of the O(2) ions (shown as purple spheres). From the BVS analysis of single crystal X-ray refinements, it was found the O(2) was overbonded; it appears that the lone-pair electrons have the greatest impact on this site. A comparison of the structures of $Ca_{10}(PO_4)_6Cl_2$ with $Ca_4Pb_6(PO_4)_6Cl_2$, which contains Ca exclusively at the A^F site, shows a similar arrangement of the O(2) ions. To accommodate the lone pair electrons in the Pb^F polyhedra, the O(2) ions are forced into a position that results in a larger metaprism twist angle. Alternatively, the displacement of the O(2) ion could be an indication that the Pb-O polyhedra are much more distorted than presently modelled and the structure may adopt the low symmetry structure found for the monoclinic polymorph.

In the lacunar apatite $Pb_9(PO)_6$, the lone pair electrons at the Pb^T sites are supporting the channel because no *X* ions are present. In $Pb_{10}(PO_4)_6Cl_2$ and $Ca_4Pb_6(PO_4)_6Cl_2$ the channel is filled with

both the Cl ions and the lone pair electrons and it is clear that when compared to $Ca_{10}(PO_4)_6Cl_2$, these structures possess a visibly expanded channel. The lacunar apatites generally have the largest twist angles found in apatites, even larger than the 24-25° observed in the triclinically distorted apatite of Baikie *et al*. (2007). The triclinic distortion only appears if the channel site is fully occupied. In the lacunar apatites, the channel is occupied only by Pb^T lone pairs, which allow the channel to contract more than the framework and the achievement of large twist angles, without loss of hexagonal symmetry.

4. Conclusions

A single-crystal synchrotron X-ray diffraction study has confirmed a superstructure for mimetite that provides a means to accommodate stereochemically active lone pair electrons at the Pb^F sites. In addition, a variable-temperature single-crystal X-ray diffraction study of vanadinite, pyromorphite and finnemanite suggests that the superstructure might be a structural adaption common to all Pb-containing apatites. The latter suggestion is supported by evidence from powder synchrotron X-ray diffraction that confirms that the superstructure exists up to $x = 0.5$ in the $Pb_{10}(As_{1-x}PO_4)_6Cl_2$ synthetic solid-solution. It appears that stereochemically active electron lone-pairs in lead apatites are analogous to interstitial oxygen in superstoichiometric silicate and germanate analogues, and occupy the same void spaces.

5. Acknowledgements

The authors would like to thank Professor Allan Pring at the South Australian museum for providing samples of the lead apatite minerals investigated in this study. We would also like to acknowledge the Agency for Science, Technology and Research (A*STAR) PSF grant 082 101 0021 ‘Optimization of Oxygen Sublattices in Solid Oxide Fuel Cell Apatite Electrolytes’ for funding the work and the Ministry of Education (MOE) Tier 2 grant T208B1212 for enabling the purchase of a single crystal X-ray diffractometer. Analytical assistance was provided by the Facility of Analysis, Characterisation, Testing and Simulation (FACTS) at Nanyang Technological University.

Figures and Tables

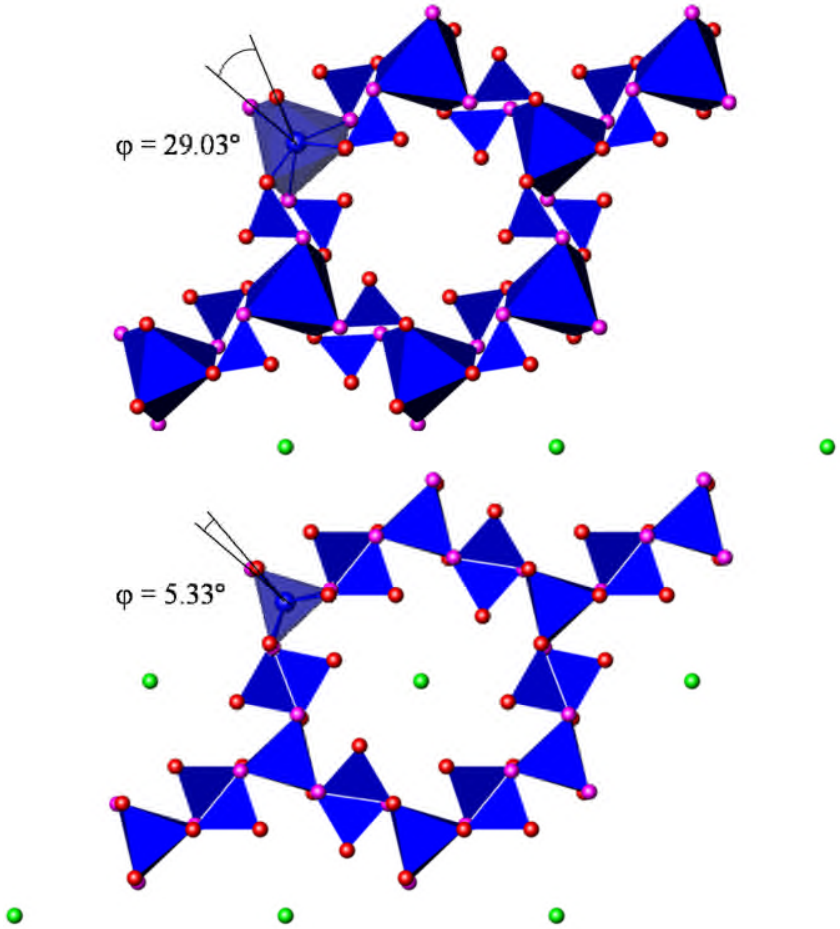

Figure 1. Representation of the upper and lower limits of metaprism twist angle (φ) found in Pb containing apatites. (Top) The lacunary apatite $Pb_8K_2(PO_4)_6$ (Mathew *et al.*, 1980) and (Bottom) phosphohedyphane, $Ca_4Pb_6(PO_4)_6Cl_2$ (Rouse *et al.*, 1984). The O(2) oxygen ions are shown as purple spheres.

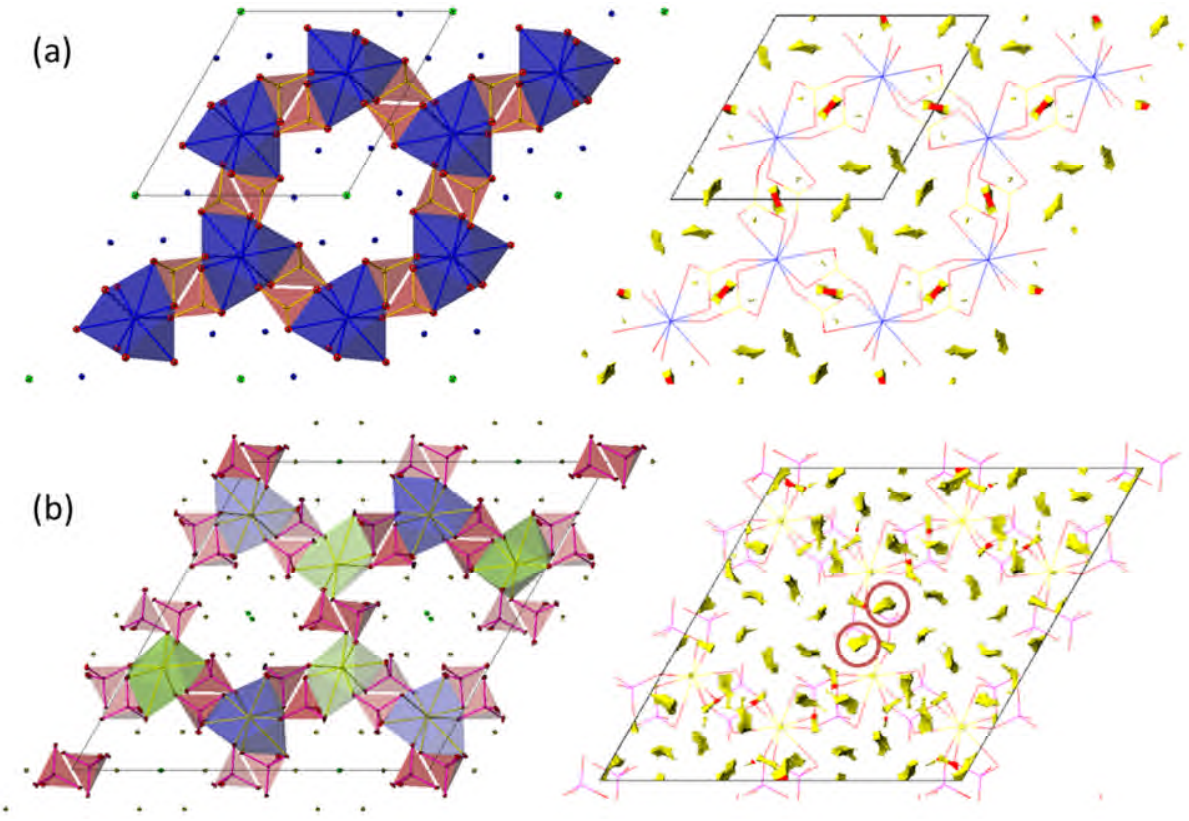

Figure 2. Polyhedral representations of the refined structures of (a) vanadinite and (b) mimetite that were derived from single crystal X-ray diffraction data collected at ambient temperature. The images on the right are the voids within the apatite structure that were calculated using the software Atoms (Dowty, 2002) and reveal the different locations of the lone pair electrons in the conventional hexagonal $P6_3/m$ and monoclinic superstructures.

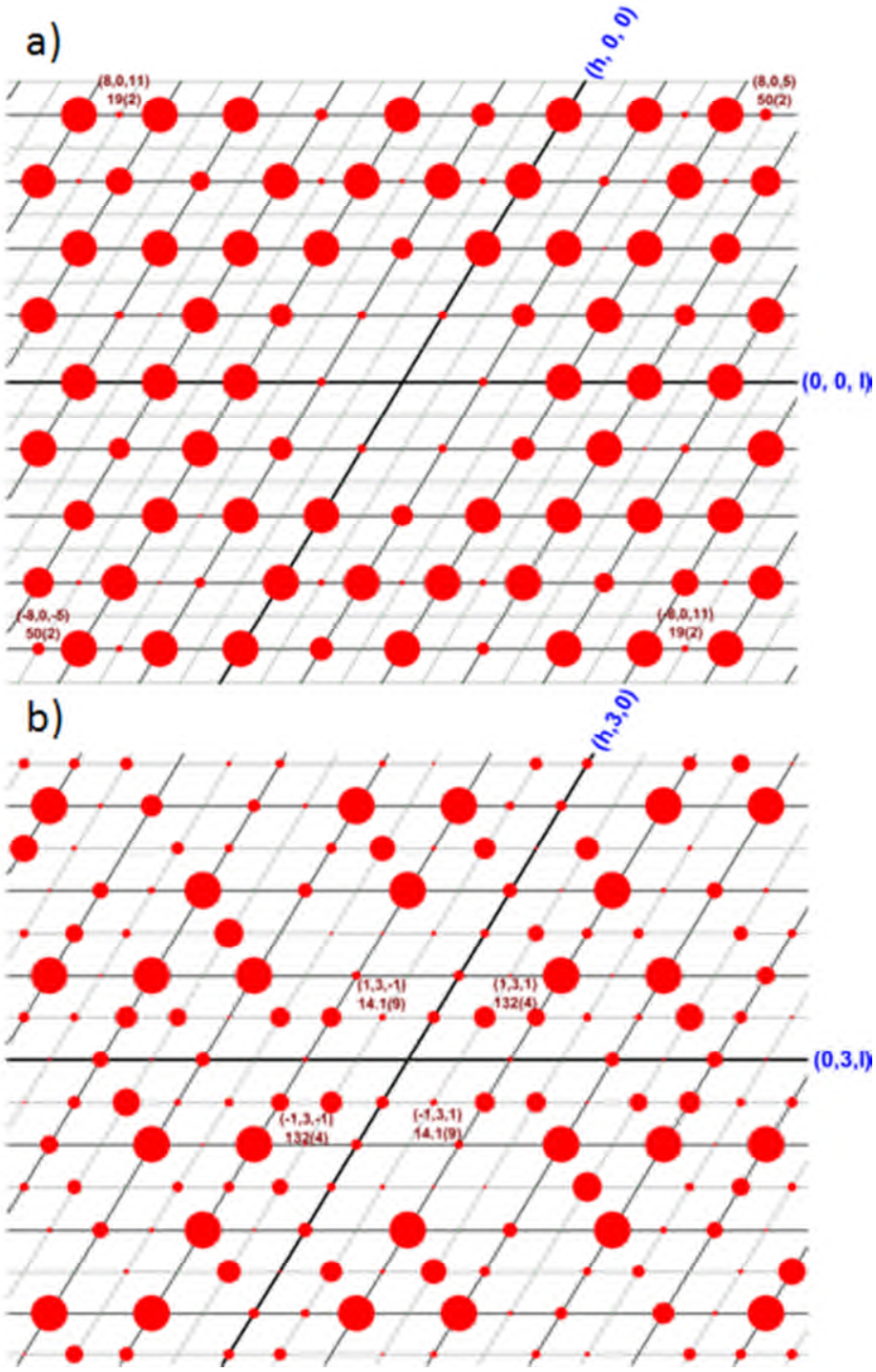

Figure 3. Reciprocal space views of I_{obs} for b^* at a) $k = 0$ and b) $k = 3$. All even numbered reflections (h 0 l) and (h 3 l) correspond to the original cell, while all odd numbered reflections correspond to the supercell.

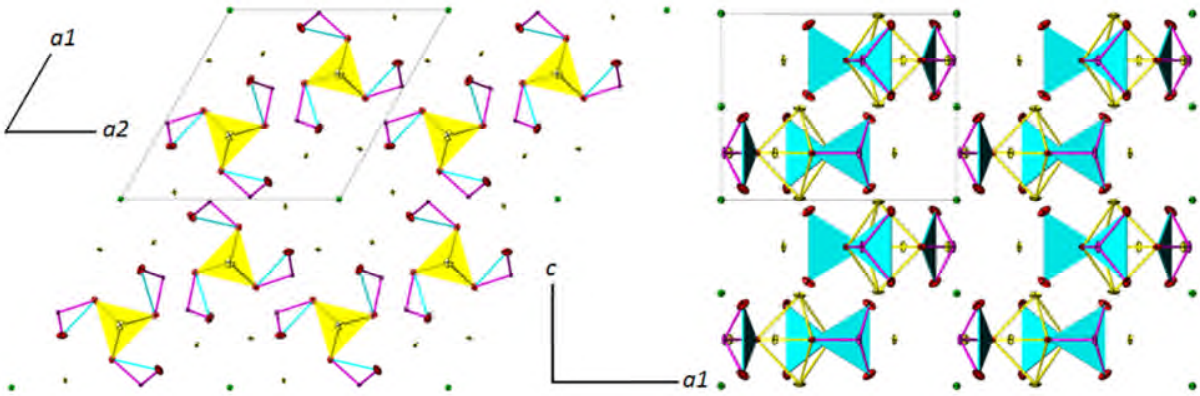

Figure 4. Structural representation of the refined room temperature structure of finnemanite. The anisotropic displacement elipsoids are shown with 50% probability.

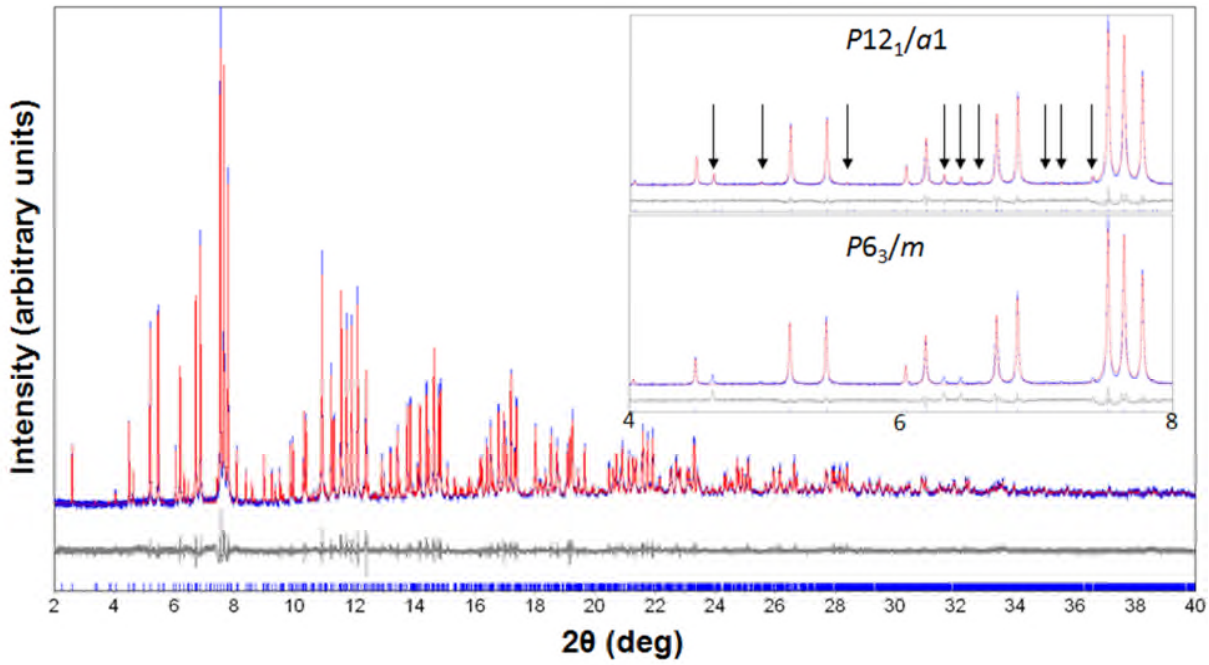

Figure 5. Rietveld refinement of the powder synchrotron data of synthetic mimetite where the observed pattern is shown in blue, the calculated in blue and the difference plot in grey. Inset – Expanded region with black arrows indicating the supercell reflections that are unaccounted for in hexagonal $P6_3/m$ model.

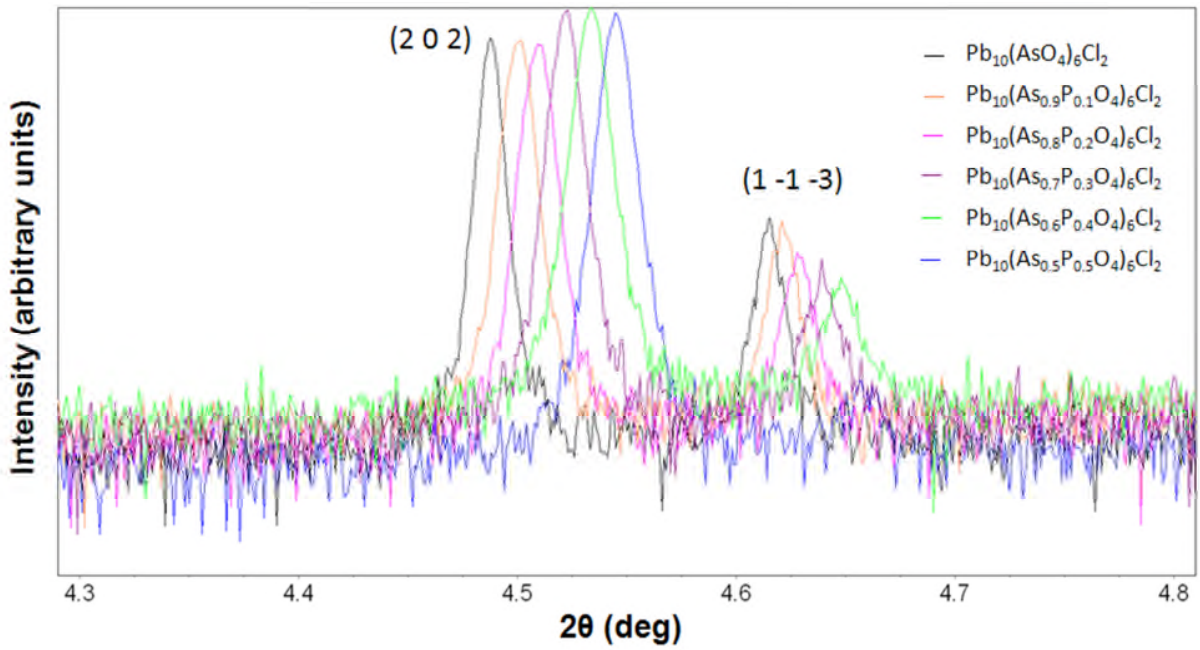

Figure 6. Disappearance of the supercell reflection with increasing values of x in the $Pb_{10}(As_{1-x}PO_4)_6Cl_2$ solid solution. For $x = 0.5$ the (1 -1 -3) reflection is absent, indicating that $Pb_{10}(As_{0.5}P_{0.5}O_4)_6Cl_2$ adopts the conventional hexagonal $P6_3/m$ apatite structure at room temperature.

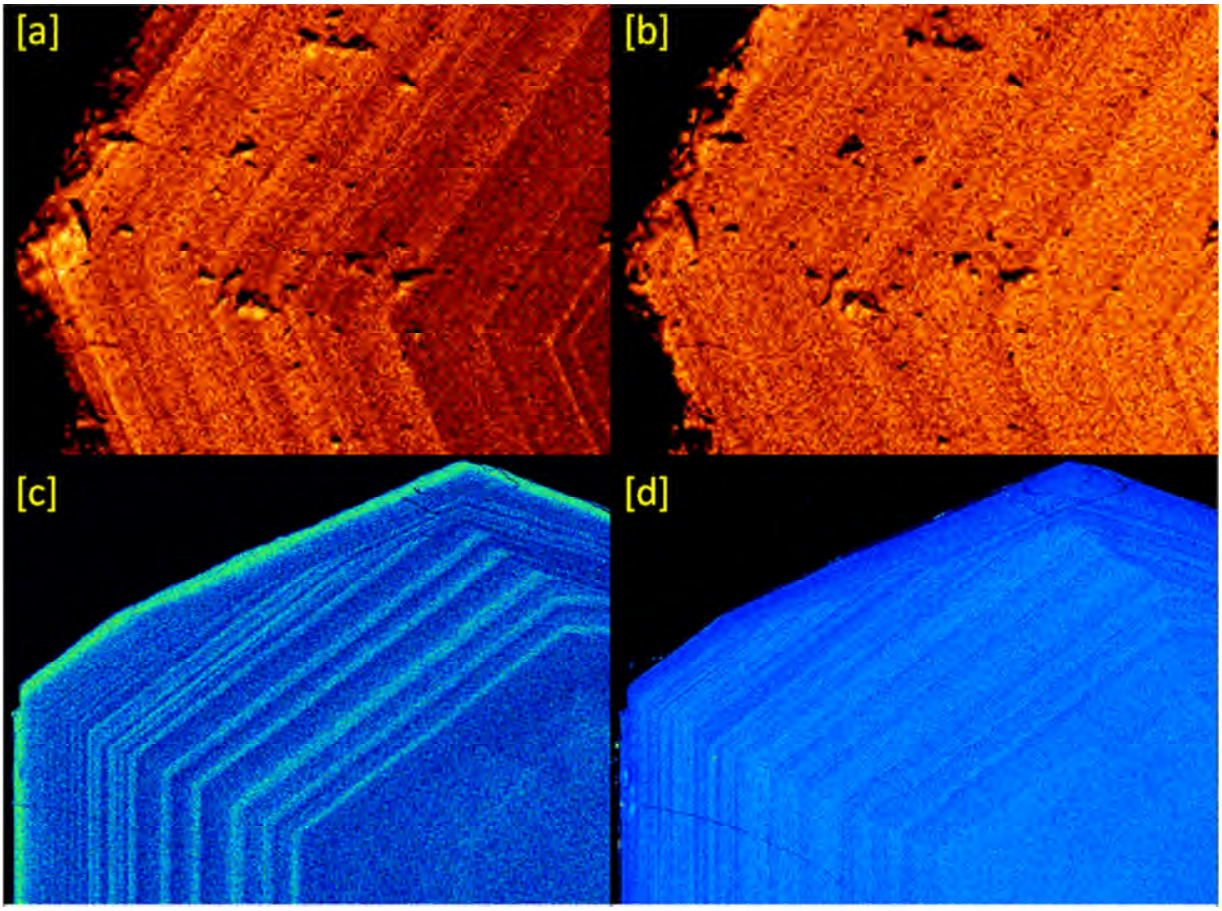

Figure 7. Chemical zoning of mimetite; [a] and [b] showing the P and V zoning for vanadinite with the elemental maps obtained from SEM; [c] P zoning [d] Ca zoning derived from elemental mapping from the EPMA measurements, with. EBSD showed that the vanadinite is orientated with the sample surface ⊥ *c*-axis, while in mimetite, the *c*-axis (*b*-axis of the monoclinic supercell) is inclined at 40.5° (±0.5) to the plane of the sample surface.

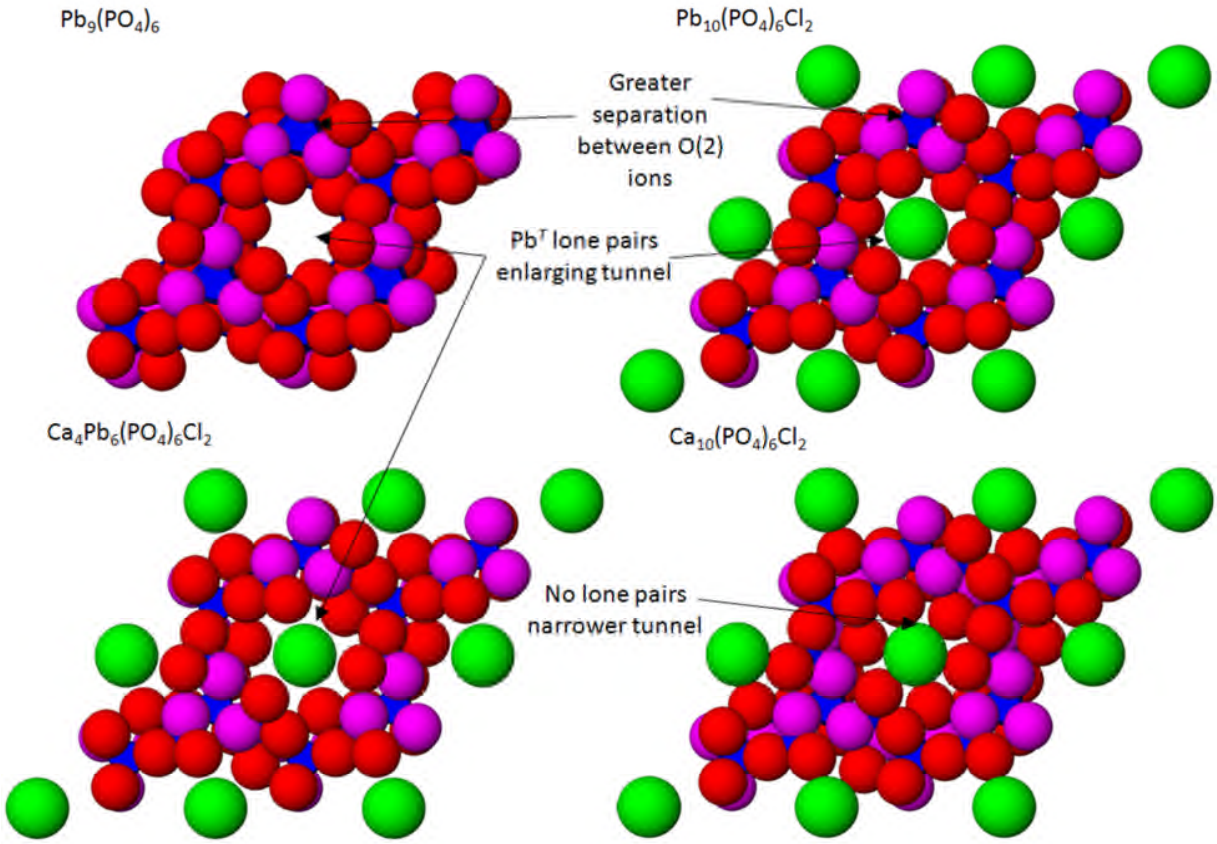

Figure 8. Structural representations of the phosphate apatites $Pb_9(PO_4)_6$, $Pb_{10}(PO_4)_6Cl_2$, $Ca_4Pb_6(PO_4)_6Cl_2$ and $Ca_{10}(PO_4)_6Cl_2$. Realistic ionic radii (Shannon, 1976) have been used in their construction so that the different packing of ions and the effects of the stereochemically active lone pairs present at both the Pb^F and Pb^T sites are clear. The O(2) ions are shown as purple spheres with the remaining oxygen shown in red. The Cl are represented by green spheres.

Table 1. Summary of atomic bond valence sums for room temperature $P6_3/m$ refinements of the Pb-apatite minerals (*B* = tetrahedral cation)

	Vanadinite	**Pyromorphite**	**Mimetite**	**Finnemanite**
Pb^F	1.95(2)	1.960(15)	1.82(2)	1.83(3)
Pb^T	1.98(2)	1.976(14)	1.90(3)	1.98(2)
B	5.13(7)	4.84(5)	5.25(10)	3.23(6)
O(1)	2.03(6)	1.86(4)	2.03(7)	-
O(2)	2.15(3)	2.15(3)	2.18(5)	2.29(4)
O(3)	1.98(3)	1.85(2)	1.89(5)	1.86(3)
Cl	1.1019(6)	1.2487(6)	1.1218(9)	1.2429(10)

R_o values used for the bond valence summations Pb^{2+}-O = 2.112; V^{5+}-O = 1.799; P^{5+}-O = 1.617; As^{5+}-O = 1.767; As^{3+}-O = 1.789 Pb^{2+}-Cl = 2.53

Table 2. Bond valence summary of the mimetite supercell.

Pb^F(1)	1.946(14)	**As(5)**	4.99(5)	**O(4a)**	1.87(2)
Pb^F(2)	1.956(14)	**As(6)**	5.04(5)	**O(4b)**	2.03(2)
Pb^F(3)	1.911(14)	**O(1a)**	2.04(2)	**O(4c)**	1.86(2)
Pb^F(4)	1.973(14)	**O(1b)**	1.94(2)	**O(4d)**	2.08(3)
Pb^T(1)	2.054(15)	**O(1c)**	1.85(2)	**O(5a)**	1.99(2)
Pb^T(2)	2.068(17)	**O(1d)**	2.07(3)	**O(5b)**	1.87(2)
Pb^T(3)	1.962(14)	**O(2a)**	2.01(3)	**O(5c)**	1.99(2)
Pb^T(4)	2.044(17)	**O(2b)**	2.00(3)	**O(5d)**	2.03(2)
Pb^T(5)	1.973(15)	**O(2c)**	1.86(3)	**O(6a)**	1.93(2)
Pb^T(6)	2.058(16)	**O(2d)**	2.06(3)	**O(6b)**	2.08(3)
As(1)	4.93(5)	**O(3a)**	2.00(4)	**O(6c)**	2.08(2)
As(2)	4.99(5)	**O(3b)**	2.08(2)	**O(6d)**	1.92(3)
As(3)	4.95(5)	**O(3c)**	2.03(2)	**Cl(1)**	1.145(3)
As(4)	4.96(5)	**O(3d)**	1.74(2)	**Cl(2)**	1.138(3)

Table 3. Composition of vanadinite, pyromorphite, mimetite and finnemanite derived from EDX.

	Mimetite				***Pyromorphite***			
	Pb (wt%)	**As (wt%)**	**Cl (wt%)**	**O (wt%)**	**Pb (wt%)**	**P (wt%)**	**Cl (wt%)**	**O (wt%)**
Mean	69.09	15.49	2.35	13.08*	77.75	6.17	2.73	13.35*
Stdev	0.26	0.20	0.08		0.11	0.05	0.5	
Ideal	69.61	15.10	2.38	12.90	76.38	6.85	2.61	14.15
% diff	-0.76%	2.57%	-1.51%		1.79%	-9.96%	4.40%	
	***Vanadinite*[(1)]**				***Finnemanite*[(2)]**			
	Pb(wt%)	**V (wt%)**	**Cl (wt%)**	**O (wt%)**	**Pb (wt%)**	**As (wt%)**	**Cl (wt%)**	**O (wt%)**
Mean	73.67	10.42	2.64	13.27*	71.92	15.53	2.61	9.94*
Stdev	0.19	0.13	0.10		0.21	0.17	0.04	
Ideal	73.15	10.79	2.50	13.56	77.48	20.60	2.46	10.00
% diff	0.71%	5.45%	-3.46%		-0.02%	-0.52%	6.10%	

[(1)] EDX identified approximately 0.1-0.4wt% P in vanadinite; [(2)] and 0.2-0.3wt% Sb and Fe in the finnemanite

Table 4. Composition of mimetite analysed by EPMA and expressed as wt% normalized to 100 together with 1 sigma standard deviation of 10 repeat analyses. For elements below detection limits, a 3 sigma detection limit is reported.

Pb (wt%)	As (wt%)	O (wt%)	Cl (wt%)	Ca (wt%)	P (wt%)
70.16 ±0.58	13.99 ±0.38	12.84 ±0.24	2.74 ±0.14	0.19 ±0.04	0.07 ±0.03

Na	F	Mg	Sb	Si	V	S	Ti
<251 ppm	<120 ppm	<111 ppm	<51 ppm	<48 ppm	<31 ppm	<30 ppm	<25 ppm

Table 5. Selected crystal structure data from the literature for Pb-containing apatites. Unless indicated, all data were obtained from single crystal X-ray diffraction.

Formula	*a*	*c*	Vol	*c*/*a*	Average ionic radii	Twist (φ)	Reference
$Pb_{10}(PO_4)_6F_2$	9.760(8)	7.300(8)	602.22	0.7480	1.1488	23.6	(Belokoneva *et al.*, 1982)
$Pb_{10}(PO_4)_6(OH)_2$	9.774(1)	7.291(1)	603.20	0.7460	1.1498	22.1	(Barinova *et al.*, 1998)
$Pb_{10}(PO)_6Cl_2$	9.976(1)	7.351(2)	633.62	0.7369	1.1602	17.6	(Dai and Hughes, 1989)
$Pb_{10}(VO_4)_6Cl_2$	10.317(3)	7.338(3)	676.45	0.7113	1.1874	17.7	(Dai and Hughes, 1989)
$Pb_{9.85}(VO_4)_6I_{1.7}$	10.422(5)	7.467(3)	702.39	0.7166	1.2050	16.7	(Audubert *et al.*, 1999)
$Pb_{10}(AsO_4)_6Cl_2$	10.250(2)	7.454(1)	678.22	0.7272	1.1845	18.8	(Calos and Kennard, 1990)
$Pb_{10}(AsO_4)_6Cl_{1.48}O_{0.26}$ [#]	10.206(1)	7.448(1)	671.83	0.7298	1.1831	19.9	(Baikie *et al.*, 2008)
$Pb_{10}(PO_4)_6O$	9.865(1)	7.431(1)	626.25	0.7532	1.1785	21.0	(Krivovichev and Burns, 2003)
$Pb_{10}(VO_4)_4(GeO_4)_2$	10.097(3)	7.396(2)	653.00	0.7325	1.1790	26.6	(Ivanov and Zavodnik, 1989)
$Pb_{10}(VO_4)_4(SiO_4)_2$	9.987(1)	7.360(1)	635.70	0.7370	1.1729	25.7	(Krivovichev *et al.*, 2004)
$Pb_{10}(GeO_4)_4(CrO_4)_2$	10.105(3)	7.428(2)	656.86	0.7351	1.1757	25.8	(Engel and Deppisch, 1988)
$Pb_{10}(GeO_4)_4(SO_4)_2$	10.058(4)	7.416(1)	649.72	0.7373	1.1690	25.2	(Engel and Deppisch, 1988)
$Pb_8K_2(PO_4)_6$	9.872(1)	7.304(1)	610.85	0.7433	1.1623	28.8	(Mathew *et al.*, 1980)
$Pb_8K_2(VO_4)_6$	10.142(4)	7.472(3)	665.60	0.7367	1.1881	29.0	(Azrour *et al.*, 1998)
$Pb_8Na_2(PO_4)_6$	9.725(1)	7.190(1)	588.88	0.7393	1.1452	24.0	(Koumiri *et al.*, 2000)
$Pb_8Na_2(VO_4)_6$	10.059(1)	7.330(1)	642.31	0.7287	1.1724	26.2	(Azrour *et al.*, 1998)
$Bi_{1.6}Na_{3.6}Pb_{4.8}(PO_4)_6$	9.684(1)	7.168(1)	582.15	0.7402	1.1348	22.8	(Hamdi *et al.*, 2006)
$Pb_9(PO_4)_6$	9.826(4)	7.357(3)	615.16	0.7487	1.1471	27.3	(Hata *et al.*, 1980)
$Ca_2Na_2Pb_6(PO_4)_6$	9.658(8)	7.081(6)	572.01	0.7332	1.1368	9.7	(Naddari *et al.*, 2003)
$Ca_2Li_2Pb_6(PO_4)_6$ [*]	9.679(2)	7.113(1)	577.09	0.7349	1.1244	13.6	(Naddari *et al.*, 2002)
$Ca_{3.68}Pb_{6.32}(P_{0.91}As_{0.09}O_4)_6Cl_2$	9.857(1)	7.130(2)	599.94	0.7233	1.1475	8.6	(Kampf *et al.*, 2006)
$Ca_4Pb_6(As_{0.98}P_{0.02}O_4)_6Cl_2$	10.140(3)	7.185(4)	639.78	0.7086	1.1678	5.3	(Rouse *et al.*, 1984)
$Na_6Pb_4(SO_4)_6Cl_2$	9.81(2)	7.14(2)	595.07	0.7278	1.1345	13.4	(Schneider, 1967)
$Ca_{1.62}Pb_{8.38}(PO_4)_6(OH)_2$ [*]	9.769(2)	7.320(2)	604.98	0.7493	1.1438	18.1	(Bigi *et al.*, 1989)
$Ca_{5.58}Pb_{4.42}(PO_4)_6(OH)_2$ [*]	9.609(2)	7.077(2)	565.90	0.7365	1.1268	13.7	"
$Ca_{7.86}Pb_{2.14}(PO_4)_6(OH)_2$ [*]	9.491(2)	6.953(2)	542.42	0.7326	1.1162	16.6	"

$Ca_3Pb_7(VO_4)_6F_{1.06}O_{0.47}$*	10.053(1)	7.303(1)	639.22	0.7265	1.1638	11.8	(Dong and White, 2004b)
$Ca_{4.45}Pb_{5.55}(VO_4)_6F_{1.36}O_{0.32}$*	10.023(1)	7.241(1)	630.02	0.7224	1.1575	15.2	(Dong and White, 2004b)
$Ca_{5.1}Pb_{4.9}(VO_4)_6F_{0.6}O_{0.7}$*	10.001(1)	7.199(1)	623.62	0.7199	1.1551	16.1	(Dong and White, 2004a)
$Ca_{5.22}Pb_{4.78}(VO_4)_6F_{0.6}O_{0.7}$*	10.003(1)	7.186(1)	622.62	0.7184	1.1548	14.5	(Dong and White, 2004a)
$Ca_{5.24}Pb_{4.76}(VO_4)_6F_{0.6}O_{0.7}$*	10.002(1)	7.188(1)	622.80	0.7186	1.1547	14.4	(Dong and White, 2004a)
$Ca_{5.38}Pb_{4.62}(VO_4)_6F_2$*	9.946(1)	7.198(1)	616.70	0.7237	1.1528	22.0	(Dong and White, 2004a)
$Ca_{5.58}Pb_{4.42}(VO_4)_6F_{1.7}O_{0.15}$*	9.986(1)	7.183(1)	620.23	0.7193	1.1523	18.5	(Dong and White, 2004b)
$Ca_{6.18}Pb_{3.82}(VO_4)_6F_{1.46}O_{0.27}$*	9.956(1)	7.181(1)	613.83	0.7213	1.1497	19.7	(Dong and White, 2004b)
$Ca_{6.94}Pb_{3.06}(VO_4)_6F_{1.7}O_{0.15}$*	9.917(1)	7.120(1)	606.46	0.7179	1.1463	18.5	(Dong and White, 2004b)
$Ca_{6.99}Pb_{3.01}(VO_4)_6F_{1.58}O_{0.21}$*	9.918(1)	7.115(1)	606.09	0.7175	1.1460	23.3	(Dong and White, 2004b)
$Ca_{8.24}Pb_{1.76}(VO_4)_6F_{1.5}O_{0.25}$*	9.844(1)	7.064(1)	592.79	0.7175	1.1404	20.4	(Dong and White, 2004b)
$Ca_{8.67}Pb_{1.33}(VO_4)_6F_{1.62}O_{0.19}$*	9.821(1)	7.052(1)	589.04	0.7181	1.1384	22.3	(Dong and White, 2004b)
$Ca_{9.43}Pb_{0.57}(VO_4)_6F_{1.8}O_{0.1}$*	9.784(1)	7.032(1)	582.89	0.7187	1.1351	21.7	(Dong and White, 2004b)

* Structure determined from powder X-ray diffraction data except # powder neutron diffraction data

Table 6. Crystal chemical formula of Pb solid solutions.

Formula	*A*-site cation distribution
$Ca_{1.62}Pb_{8.38}(PO_4)_6(OH)_2$	$[Ca_{1.46}Pb_{2.54}]^F[Ca_{0.16}Pb_{5.84}]^T$
$Ca_{5.58}Pb_{4.42}(PO_4)_6(OH)_2$	$[Ca_{3.74}Pb_{0.26}]^F[Ca_{1.74}Pb_{4.26}]^T$
$Ca_{7.86}Pb_{2.14}(PO_4)_6(OH)_2$	$[Ca_{3.86}Pb_{0.14}]^F[Ca_{3.96}Pb_{2.04}]^T$
$Ca_3Pb_7(VO_4)_6F_{1.06}O_{0.47}$	$[Ca_{2.32}Pb_{1.68}]^F[Ca_{0.72}Pb_{5.28}]^T$
$Ca_{4.45}Pb_{5.55}(VO_4)_6F_{1.36}O_{0.32}$	$[Ca_{2.76}Pb_{1.24}]^F[Ca_{1.68}Pb_{4.32}]^T$
$Ca_{5.1}Pb_{4.9}(VO_4)_6F_{0.6}O_{0.7}$	$[Ca_{2.88}Pb_{1.12}]^F[Ca_{2.22}Pb_{3.78}]^T$
$Ca_{5.22}Pb_{4.78}(VO_4)_6F_{0.6}O_{0.7}$	$[Ca_{3.36}Pb_{0.64}]^F[Ca_{1.86}Pb_{4.14}]^T$
$Ca_{5.24}Pb_{4.76}(VO_4)_6F_{0.6}O_{0.7}$	$[Ca_{3.32}Pb_{0.68}]^F[Ca_{1.92}Pb_{4.08}]^T$
$Ca_{5.38}Pb_{4.62}(VO_4)_6F_2$	$[Ca_{2.44}Pb_{1.56}]^F[Ca_{2.94}Pb_{3.06}]^T$
$Ca_{5.58}Pb_{4.42}(VO_4)_6F_{1.7}O_{0.15}$	$[Ca_{3.12}Pb_{0.88}]^F[Ca_{2.46}Pb_{3.54}]^T$
$Ca_{6.18}Pb_{3.82}(VO_4)_6F_{1.46}O_{0.27}$	$[Ca_{3.12}Pb_{0.88}]^F[Ca_{3.06}Pb_{2.94}]^T$
$Ca_{6.94}Pb_{3.06}(VO_4)_6F_{1.7}O_{0.15}$	$[Ca_{3.28}Pb_{0.72}]^F[Ca_{3.66}Pb_{2.34}]^T$
$Ca_{6.99}Pb_{3.01}(VO_4)_6F_{1.58}O_{0.21}$	$[Ca_{3.16}Pb_{0.84}]^F[Ca_{3.84}Pb_{2.16}]^T$
$Ca_{8.24}Pb_{1.76}(VO_4)_6F_{1.5}O_{0.25}$	$[Ca_{3.60}Pb_{0.40}]^F[Ca_{4.68}Pb_{1.32}]^T$
$Ca_{8.67}Pb_{1.33}(VO_4)_6F_{1.62}O_{0.19}$	$[Ca_{3.68}Pb_{0.32}]^F[Ca_{5.04}Pb_{0.96}]^T$
$Ca_{9.43}Pb_{0.57}(VO_4)_6F_{1.8}O_{0.1}$	$[Ca_{3.88}Pb_{0.12}]^F[Ca_{5.58}Pb_{0.42}]^T$

References

Aminoff, G. (1923) Finnemanit, ett nytt blyarsenit från Långban (Finnemanite, a new lead arsenite from Långban). Geologiska Föreningen i Stockholm Förhandlingar, 45, 160-163.

Aminoff, G., and Parsons, A.L. (1927) Symmetry and lattice dimensions of finnemanite and mimetite. Geologiska Föreningen i Stockholm Förhandlingar, 49, 438-440.

Andersson, S., and Åstrom, A. (1972) The stereochemistry of the inert pair in some solid oxides or oxide fluorides of Sb^{3+}, Bi^{3+} and Pb^{2+}. Proceedings of 5th Materials Research Symposium, 364, p. 3-14, National Bureau of Standards Special Publication 164.

Audubert, F., Savariault, J.M., and Lacout, J.L. (1999) Pentaleadtris (vanadate) iodide, a defect vanadinite-type compound. Acta Crystallographica C, 55, 271-273.

Azrour, M., El Ammari, L., Le Fur, Y., and Elouadi, B. (1998) Etude structurale d'orthovanadates d'alcalins et de plomb cristalisant avecla structure apatite lacunaire. Journal of Solid State Chemistry, 141, 373-377.

Bahfenne, S., and Frost, R.L. (2010) Raman spectroscopic study of the mineral finnemanite $Pb_5(As^{3+}O_3)_3Cl$. Journal of Raman Spectroscopy, 41, 329-333.

Baikie, T., Fang, Y., Kadro, J.M., Schreyer, M.K., Wei, F., Mhaisalkar, S., Graetzel, M., and White, T.J. (2013) Synthesis and crystal chemistry of the hybrid perovskite (CH3NH3)PbI3 for solid state sensitised solar cell applications. Journal of Materials Chemistry A, 1, 5628-5641.

Baikie, T., Ferraris, C., Klooster, W.T., Madhavi, S., Pramana, S.S., Pring, A., and Schmidt, G. (2008) The crystal chemistry and mimetite ($Pb_{10}(AsO_4)_6Cl_{1.48}O_{0.26}$) and finnemanite ($Pb_{10}(AsO_3)_6Cl_2$). Acta Crystallographica B, 64, 34-41.

Baikie, T., Mercier, P.H.J., Elcombe, M.M., Kim, J.Y., Page, Y.L., Mitchell, L.D., and White, T.J. (2007) Triclinic Apatites. Acta Crystallographica B, 63, 251-256.

Baikie, T., Pramana, S.S., Ferraris, C., Huang, Y., Kendrick, E., Knight, K.S., Ahmad, Z., and White, T.J. (2010) Polysomatic apatites. Acta. Crystallographica B, 66, 1-16.

Barinova, A.V., Bonin, M., Pushcharovskii, D.Y., Rastsvetaeva, R.K., Schenk, K., and Dimitrova, O.V. (1998) Crystal structure of synthetic hydroxylpyromorphyte $Pb_5(PO_4)_3(OH)$. Kristallografiya, 42, 224-227.

Béchade, E., Masson, O., Iwata, Y., Julien, I., Fukuda, K., Thomas, P., and Champion, E. (2009) Diffusion path and conduction mechanism of oxide ions in apatite-type lanthanum silicates. Chemistry of Materials, 21(12), 2508-2517.

Belokoneva, E.L., Troneva, E.A., Dem'yanets, L.N., Duderov, N.G., and Belov, N.V. (1982) Crystal structure of synthetic fluoropyromorphite $Pb_5(PO_4)_3F$. Kristallografiya, 27, 793-794.

Biagioni, C., and Pasero, M. (2013) The crystal structure of johnbaumite, $Ca_5(AsO_4)_3OH$, the arsenate analogue of hydroxyapatite. American Mineralogist, 98, 1580-1584.

Bigi, A., Ripamonti, A., Brückner, S., Gazzano, M., Roveri, N., and Thomas, S.A. (1989) Structure refinements of lead-substituted calcium hydroxyapatite by X-ray powder fitting. Acta Crystallographica B, 45, 247-251.

Bruker. (2008) Topas Version 4.1. Bruker AXS Inc., Madison, Wisconsin, USA.

Calos, N.J., and Kennard, C.H.L. (1990) Crystal structure of mimetite, $Pb_5(AsO_4)_3Cl$. Zeitschrift für Kristallographie, 191, 125-129.

Carlson, S., Norrestam, R., Holstam, D., and Spengler, R. (1997) The crystal structure of ganomalite $Pb_9Ca_{5.44}Mn_{0.56}Si_9O_{33}$. Zeitschrift für Kristallographie, 212, 208-212.

Dai, Y.S., and Hughes, J.M. (1989) Crystal structure refinements of vanadinite and pyromorphite. Canadian Mineralogist, 27, 189-192.

Dai, Y.S., Hughes, J.M., and Moore, P.B. (1991) The crystal structures of mimetite and clinomimetite. Canadian Mineralogist, 29, 369-376.

Dong, Z., and White, T.J. (2004a) Calcium-lead fluoro-vanadinite apatites. I Disequilibrium structures. Acta Crystallographica B, 60, 138-145.

Dong, Z., and White, T.J. (2004b) Calcium-lead fluoro-vanadinite apatites. II. Equilbrium structures. Acta Crystallographica B, 60, 146-154.

Dowty, E. (2002) ATOMS Version 6.0. Shape Software, Kingsport, Tennessee.

Effenberger, H., and Pertlik, F. (1979) Die kristallstruktur des finnemanits, $Pb_5Cl(AsO_3)$, mit einem vergleich zum strukturtyp des chlorapatits $Ca_5Cl(PO_4)_3$. Tschermaks Mineralogische und Petrographische Mitteilungen, 26, 95-107.

Elliott, P. (1991) Minerals of the Beltana Mine, Puttapa, South Australia. The Mineralogical Record, 22, 449-456.

Engel, G., and Deppisch, B. (1988) Die kristallstruktur von $Pb_5(GeO_4)_2SO_4$ und $Pb_5(GeO_4)_2CrO_4$, zweier bleiapatite mit unbesetzten halogenlagen. Zeitschrift für Anorganische und Allgemeine Chemie, 562, 131-140.

Eon, J.G., Boechat, C.B., Rossi, A.M., Terra, J., and Ellis, D.E. (2006) A structural analysis of lead hydroxyvanadinite. Physical Chemistry Chemical Physics, 8, 1845-1852.

Fleet, M.E., Liu, X., and Shieh, S.R. (2010) Structural change in lead fluorapatite at high pressure. Physics and Chemistry of Minerals, 37, 1-9.

Flis, J., Borkiewicz, O., Bajda, T., Manecki, M., and Klasa, J. (2010) Synchrotron-based X-ray diffraction of the lead apatite series $Pb_{10}(PO_4)_6Cl_2$ - $Pb_{10}(AsO_4)_6Cl_2$. Journal of Synchrotron Radiation, 17, 207-214.

Gabrielson, O. (1955) The crystal structure of finnemanite $Pb_5Cl(AsO_3)_3$. Arkiv für Kemi, Mineralogi och Geologi, 2, 1-8.

Giuseppetti, G., Rossi, G., and Tadini, C. (1971) The crystal structure of nasonite. American Mineralogist, 56, 1174-1179.

Grubb, P.L.C. (1971) Mineralogy and genesis of the Beltana zinc-lead deposit, Puttapa, South Australia. Journal of the Geological Society of Australia, 18, 165-171.

Hamdi, B., El Feki, H., Salah, A.B., Salles, P., Baules, P., and Savariault, J.-M. (2006) Ionic conductivity and phase transition in $Pb_{4.8}Bi_{1.6}Na_{3.6}(PO_4)_6$, an apatite-type compound. Solid State Ionics, 177, 1413-1420.

Hata, M., Marumo, F., Iwai, S., and Aoki, H. (1980) Structure of a lead apatite $Pb_9(PO_4)_6$. Acta Crystallographica B, 36, 2128-2130.

Hendricks, S.B., Jefferson, M.E., and Mosley, V.M. (1932) The crystal structures of some natural and synthetic apatite-like substances. Zeitschrift für Kristallographie, 81, 352-369.

Holten, T., Jamtveit, B., and Meakin, P. (2000) Noise and oscillatory zoning in minerals. Geochimica et Cosmochimica Acta, 64, 1893-1904.

Ivanov, S.A., and Zavodnik, V.E. (1989) Crystal structure of $Pb_5GeV_2O_{12}$. Soviet Physics - Crystallography, 34, 493-496.

Kabsch, W. (2010) XDS. Acta Crystallographica D, 66, 125-132.

Kampf, A.R., Steele, I.M., and Jenkins, R.A. (2006) Phosphohedyphane, $Ca_2Pb_3(PO_4)_3Cl$, the phosphate analog of hedyphane: Description and crystal structure. American Mineralogist, 91, 1909-1917.

Kay, M.I., Newnham, R.E., and Wolfe, R.W. (1975) The crystal structure of the ferroelectric phase of $Pb_5Ge_3O_{11}$. Ferroelectrics, 9, 1-6.

Keppler, U. (1968) Monokliner mimetsit, $Pb_5(AsO_4)_3Cl$. Neues Jahrbuch für Mineralogie - Monatshefte 359-362.

Keppler, U. (1969) Zum modifikationswechsel chlor-haltiger apatite. Neues Jahrbuch für Mineralogie - Monatshefte, 64-67.

Koumiri, M.E., Oishi, S., Sato, S., Ammari, L.E., and Elouadi, B. (2000) The crystal structure of the lacunar apatite $NaPb_4(PO_4)_3$. Materials Research Bulletin, 35, 503-513.

Krivovichev, S.V., Armbruster, T., and Depmeier, W. (2004) One-dimensional lone electron pair micelles in the crystal structure of $Pb_5(SiO_4)(VO_4)_2$. Materials Research Bulletin, 39, 1717-1722.

Krivovichev, S.V., and Burns, P.V. (2003) Crystal chemistry of lead oxide phosphates: crystal structures of $Pb_4O(PO_4)_2$, $Pb_8O_5(PO_4)_2$ and $Pb_{10}(PO_4)_6O$. Zeitschrift für Kristallographie, 218, 357-365.

Lee, P.L., Shu, D., Ramanathan, M., Preissner, C., Wang, J., Beno, M.A., Von Dreele, R.B., Ribaud, L., Kurtz, C., Antao, S., Jiao, X., and Toby, B.H. (2008) A twelve-analyzer detector system for high-resolution powder diffraction. Journal of Synchrotron Radiation, 15, 427-432.

León-Reina, L., Losilla, E.R., Martinez-Lara, M., Bruque, S., and Aranda, M.A.G. (2004) Interstitial oxygen conduction in lanthanum oxy-apatite electrolytes. Journal of Materials Chemistry, 14, 1142-1149.

Lim, S., Baikie, T., Smith, R., Knight, K., and White, T.J. (2011) The Apatite Metaprism Twist Angle (Φ) as a Tool for Crystallochemical Diagnosis. Journal of Solid State Chemistry, 184, 2978-2986.

Mathew, M., Brown, W.E., Austin, M., and Negas, T. (1980) Lead alkali apatites without hexad anion: the crystal structure $Pb_8K_2(PO_4)_6$. Journal of Solid State Chemistry, 35, 69-76.

Mills, S.J., Ferraris, G., Kampf, A.R., and Favreau, G. (2012) Twinning in pyromorphite: The first documented occurence of twinning by merohedry in the apatite supergroup. American Mineralogist, 97, 415-418.

Momma, K., and Izumi, F. (2008) VESTA: a three-dimensional visualization system for electronic and structural analysis. Journal of Applied Crystallography, 41, 653-658.

Moore, P.B., and Shen, J. (1984) Roeblingite, $Pb_2Ca_6(SO_4)_2(OH)_2(H_2O)_4[Mn(Si_3O_9)_2]$: its crystal structure and comments on the lone pair effect. American Mineralogist, 69, 1173-1179.

Naddari, T., Feki, H.E., Savariault, J.M., Salles, P., and Salah, A.B. (2003) Structure and ionic conductivity of the lacunary apatite $Pb_6Ca_2Na_2(PO_4)_6$. Solid State Ionics, 158, 157-166.

Naddari, T., Savariault, J.M., Feki, H.E., Salles, P., and Salah, A.B. (2002) Conductivity and structural investigations in lacunary $Pb_6Ca_2Li_2(PO_4)_6$ apatite. Journal of Solid State Chemistry, 166, 237-244.

Noda, Y., Masumoto, K., Ohba, S., Saito, Y., Toriumi, K., Iwata, Y., and Shibuya, I. (1987) Temeprature depedence of atomic thermal parameters of lead chalcogenides, PbS, PbSe and PbTe. Acta. Crystallographica C, 43, 1443-1445.

Orera, A., Baikie, T., Kendrick, E., Shin, J.F., Pramana, S., Smith, R., White, T.J., Sanjuán, M.L., and Slater, P.R. (2011) Apatite germanates doped with tungsten: synthesis, structure, and conductivity. Dalton Transactions, 40, 3903-3908.

Palatinus, L., and Chapuis, G. (2007) Superflip - a computer program for the solution of crystal structures by charge flipping in arbitrary dimensions. Journal of Applied Crystallography, 40, 786-790.

Panchmatia, P., Orera, A., Rees, G.J., Smith, M.E., Hanna, J.V., Slater, P.R., and Islam, M.S. (2001) Elucidation of Oxygen Defects and Novel Transport Mechanisms in Apatite Fast-Ion Conductors: Combined ^{17}O NMR and Modelling Studies. Angewandte Chemie International Edition, 50, 9328-9333.

Pasero, M., Kampf, A.R., Ferraris, C., Pekov, I.V., Rakovan, J.F., and White, T.J. (2010) Nomenclature of apatite supergroup minerals. European Journal of Mineralogy, 22, 163-179.

Petriček, V., Dusek, M., and Palatinus, L. (2006) Jana2006. The crystallographic computing system., Institute of Physics, Praha, Czech Republic.

Rouse, R.C., Dunn, P.J., and Peacor, D.R. (1984) Hedyphane from Franklin, New Jersey and Långban, Sweden: cation ordering in an arsenate apatite. American Mineralogy, 89, 920-927.

Schneider, W. (1967) Caracolit, das $Na_3Pb_2(SO_4)_3Cl$ mit Apatitstruktur. Neues Jahrbuch Miner., 284-289.

Shannon, R.D. (1976) Revised effective ionic radii and systematic studies of interatomic distances in halides and chalcogenides. Acta Crystallographica A, 32, 751-767.

Shore, M., and Fowler, A.D. (1996) Oscillatory zoning in minerals: a common phenomenon. Canadian Mineralogist, 34, 1111-1126.

Sokolova, E.V., Egorov-Tismenko, Y.K., and Yakhontova, L.K. (1982) Research on crystal structures of rare arsenates: dufite and mimetite. Vestnik of Moscow university, Series 4, Geology, 50-56.

Trotter, J., and Barnes, W.H. (1958) The structure of vanadinite. Canadian Mineralogist, 6, 161-173.

Walsh, A., Payne, D.J., Egdell, R.G., and Watson, G.W. (2011) Stereochemistry of post-transition metal oxides: revision of the classical lone pair model. Chemical Society Reviews, 40, 4455-4463.

Walsh, A., and Watson, G.W. (2005) The origin of the stereochemically active Pb(II) lone pair: DFT calculations of PbO and PbS. Journal of Solid State Chemistry, 178, 1422-1428.

White, T.J., and Dong, Z. (2003) Structural derivation and crystal chemistry of apatites. Acta Crystallographica B, 59, 1-16.

White, T.J., and Toor, I.A. (1996) Stabilizing toxic metal concentrates using SMITE. Journal of the Minerals Metals & Materials Society, 48, 54-58.

Yang, Z., Ding, K., de Fourestier, J., and Li, H. (2013) The crystal structure of mimetite-2M, a new polymorph of mimetite from Xianghualing tin-polymetalic orefield, Hunan Province, R. R. China. Neues Jahrbuch für Mineralogie - Abhandlungen: Journal of Mineralogy and Geochemistry, 190(2), 229-235.